Journal of Materials Chemistry A

PAPER

View Article Online
View Journal | View Issue

Cite this: J. Mater. Chem. A, 2015, 3, 17412

Facile synthesis of rutile TiO_2 mesocrystals with enhanced sodium storage properties†

Zhensheng Hong,*[a] Kaiqiang Zhou,[a] Junwen Zhang,[a] Zhigao Huang[a] and Mingdeng Wei*[bc]

Received 11th June 2015
Accepted 27th July 2015

DOI: 10.1039/c5ta04232a

www.rsc.org/MaterialsA

With the aim of developing high performance anode (negative) materials for sodium ion batteries (NIBs), rutile TiO_2 with mesocrystalline structure were designed and used for enhancing the discharge capacity and reaction kinetics. The nanoporous rutile TiO_2 mesocrystals constructed by crystallographically oriented nanoparticle subunits with tunable microstructures were successfully prepared *via* a facile synthesis route. Such rutile TiO_2 architecture possesses a large surface area (157 m^2 g^{-1}), nanoporous nature and single-crystal-like structure, which could provide a high level of accessibility for the electrolyte and more active sites, and allow the fast electron and ion transport compared with the irregularly oriented nanoparticles. When evaluated as an anode material for sodium-ion storage, this unique architecture exhibited a high reversible capacity over 350 mA h g^{-1} at 50 mA g^{-1}, superior rate capability with a stable capacity of 151 mA h g^{-1} at 2 A g^{-1} and good cycling stability.

1. Introduction

Na-ion batteries (NIBs) have recently attracted great interest as sodium is a cheaper and more abundant alkali metal element compared to lithium.[1–4] However, it is difficult to find suitable electrode materials for NIBs to allow reversible and rapid ion insertion and extraction due to a larger diameter of the Na-ion (0.97 Å) compared to the Li-ion (0.68 Å).[5] In particular, developing new materials or nanostructures as anode (negative) materials for NIBs is receiving a high level of scientific attention. Some carbonaceous materials and partially graphitic nanostructures were used as anode materials for NIBs, showing the capability of reversibly inserting and extracting sodium ions over many cycles.[6–8] Recently, some anode materials with alloy-type (Sn and SnO_2)[9,10] and conversion-type mechanisms (CuO, Co_3O_4 and MoS_2)[11–13] exhibited high initial capacity, but many of them suffered from poor cycling performance owing to the large volume change or the sluggish kinetics. Classical insertion materials such as $Na_2Ti_3O_7$ has been also demonstrated as a promising anode material with a low operating potential around 0.3 V *vs.* Na/Na^+, however such a material so far showed a rather low capacity and poor cycling stability.[14,15] Some titanate nanostructures that remain relatively unexplored in the case of Na-ion batteries were also reported.[16–18]

TiO_2 polymorphs have attracted significant attention as typical intercalation anode materials for lithium-ion batteries (LIBs) due to their intrinsic advantages in safety, low cost, and good cyclic stability.[19–22] Most recently, it was demonstrated that anatase TiO_2 nanostructures exhibited the capability to reversibly accommodate Na ions, and displayed acceptable capacity and good cycling stability.[23–28] However, the Na ion interaction properties of rutile TiO_2 nanocrystals were relatively rarely investigated.[29,30] Usui *et al.*[29] firstly report the Na ion storage properties of rutile TiO_2; in this study, this anode material showed a reversible capacity of 160 mA h g^{-1} at 50 mA g^{-1} through the Nb-doping method. Most recently, it was demonstrated that rutile TiO_2 microspheres displayed a reversible capacity of 140 mA h g^{-1} at 16.8 mA g^{-1}, but the capacity decreases seriously at a high current rate.[30] Thus, improving the discharge capacity and rate capability of rutile TiO_2 is still an urgent task.

Crystallographically oriented nanoparticle superstructures (mesocrystals) have been used for enhancing the discharge capacity and reaction kinetics in LIBs.[31] In this study, we report the successful utilization of rutile TiO_2 mesocrystals as an anode material for NIBs. The rutile TiO_2 mesocrystals exhibited a high reversible capacity over 350 mA h g^{-1} at 50 mA g^{-1} with improved initial coulombic efficiency, superior rate capability, and good cycling stability, due to the unique architecture with nanoporous nature, large surface area and single-crystal-like structure.

[a]Fujian Provincial Key Laboratory of Quantum Manipulation and New Energy Materials, College of Physics and Energy, Fujian Normal University, Fuzhou, Fujian 350108, China. E-mail: winter0514@163.com

[b]State Key Laboratory of Photocatalysis on Energy and Environment, Fuzhou University, Fuzhou, Fujian 350002, China. E-mail: wei-mingdeng@fzu.edu.cn

[c]Institute of Advanced Energy Materials, Fuzhou University, Fuzhou, Fujian 350002, China

† Electronic supplementary information (ESI) available: Detailed experimental procedures, additional SEM and TEM image, CV curves, XRD and Raman patterns. See DOI: 10.1039/c5ta04232a

2. Experimental

2.1 Materials synthesis

The rutile TiO_2 mesocrystals were synthesized through a one-step route, by modifying our previous two-step synthesis method.[32] In a typical synthesis, 1 g sodium dodecyl benzene sulfonate (SDBS) was dissolved in 50 mL 2.2 M HCl or HNO_3 solution. After the solution was stirred for a few minutes, 1 mL titanium(IV) isopropoxide (TIP) was added and kept at 80 °C for 48 h under stirring. The final products were obtained by centrifugation, washed with distilled water and ethanol for several times and dried at 60 °C overnight, and then calcined at 400 °C for 60 min in air to remove the residual organics. The samples obtained from HCl and HNO_3 solution were termed C-TiO_2-RM and N-TiO_2-RM, respectively.

2.2 Characterizations of the samples

Scanning electron microscopy (SEM, S8010 instrument) and transmission electron microscopy (TEM, FEI F20 S-TWIN instrument) were used for the morphological and structural characterization of the rutile TiO_2 mesocrystals. X-ray diffraction (XRD) patterns were recorded on a PANalytical X'Pert spectrometer using Co Kα radiation (λ = 1.78897 Å), and the data were changed to Cu Kα data. N_2 adsorption–desorption analysis was measured on a Micro-meritics TriStar II 3020 instrument (USA). The pore size distributions of the as-prepared samples were analyzed using non-local-density functional theory (NLDFT) methods. The Raman spectra were recorded on a LabRAM HR Evolution (HORIBA Jobin Yvon) with a 532 nm laser.

2.3 Electrochemical measurements

For the electrochemical measurement of Na-ion intercalation, the active materials were admixed with super-P and polyvinylidene fluoride (PVDF) binder additive in a weight ratio of 70 : 20 : 10. The mixture was spread and pressed on copper foil circular flakes as working electrodes (WE), and dried at 120 °C in vacuum for 12 h. Na-ion cells were assembled in coin-type cells (CR 2025) with a Na metal foil as the negative electrode, glass fiber separator (Whatman GF/F), and 1 M $NaClO_4$ in ethylene carbonate (EC) and diethyl carbonate (DEC) (1/1 in volume) as the electrolyte. The cells were assembled in a glove box filled with highly pure argon gas (O_2 and H_2O levels < 1 ppm), and charge/discharge tests were performed in the voltage range 0.01 to 3.0 V (Na^+/Na) on a Land automatic battery tester (Land CT 2001A, Wuhan, China). Cyclic voltammetry (CV) measurements were performed on Zennium (Zahner).

3. Results and discussion

The rutile TiO_2 mesocrystals were synthesized through a facile wet chemical route under the assistance of sodium dodecyl benzene sulfonate (SDBS). The mesocrystals obtained from HCl and HNO_3 solution were termed C-TiO_2-RM and N-TiO_2-RM, respectively. Fig. 1a shows the X-ray diffraction (XRD) patterns of as-prepared samples. All the diffraction peaks in Fig. 1a could be exclusively ascribed to tetragonal rutile TiO_2 (JCPDS 78-1509). The broadened diffraction peaks suggest a small crystallite size of the samples. The average crystallite size of C-TiO_2-RM was calculated to be approximately 11 nm (also 11 nm for N-TiO_2-RM), using the Scherer equation, based on the (110) diffraction peak. N_2 adsorption–desorption isotherm measurements were adopted to reveal the Brunauer–Emmett–Teller (BET) surface area and pore size distribution, as presented in Fig. 1b and c. The BET surface area and the pore volume of C-TiO_2-RM were determined to be 157 m^2 g^{-1} and 0.18 cm^3 g^{-1}, respectively. As depicted in Fig. 1b (inset), C-TiO_2-RM exhibits relatively ordered nanopores mainly located around 2.7 nm, analyzed using the non-local density functional theory (NLDFT) methods. As for N-TiO_2-RM (Fig. 1c), the BET surface area and pore volume were about 117 m^2 g^{-1} and 0.26 cm^3 g^{-1}, suggesting a lower surface area. However, a larger pore size mostly located around 5 nm could be observed for N-TiO_2-RM.

Low-magnification and high-magnification SEM images of C-TiO_2-RM obtained from 2.2 M HCl aqueous solution are shown in Fig. 2a and b. It is clearly shown that numerous regular nanoparticles of uniform size (100–120 nm) and quasi-square shape were formed. C-TiO_2-RM has a rough surface and porous structure; actually, it was composed of tiny nanoparticle subunits (Fig. 2b). Fig. 2c displays a typical TEM image of a single nanoparticle, which confirms that the rutile TiO_2 nanoparticle was constructed by tiny nanoparticle subunits with diameter about 5–7 nm, more HRTEM images are shown in Fig. S1.† The corresponding SAED pattern in the inset of Fig. 2c for the whole nanoparticle exhibited single-crystal-like diffractions, indicating that the building of nanoparticle subunits were highly ordered, leading to the formation of a crystallographic oriented mesocrystalline architecture (mesocrystals). Furthermore, the diffraction spots were slightly elongated, suggesting that there was a small mismatch between the

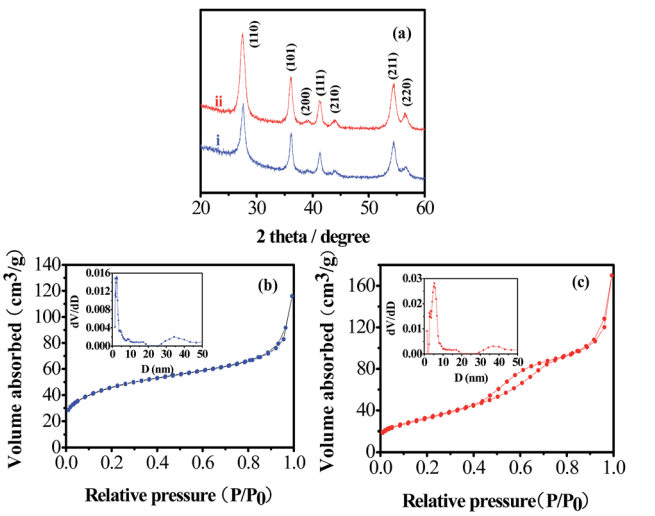

Fig. 1 (a) XRD patterns of C-TiO_2-RM (curve i) and N-TiO_2-RM (curve ii), N_2 adsorption–desorption isotherms of (b) C-TiO_2-RM and N-TiO_2-RM. The insets in (b) and (c) are the corresponding NLDFT pore size distribution.

boundaries of the nanoparticle subunits; this is usually found for the mesocrystals, which were growing by the oriented attachment route.[31,33] Moreover, the porous rutile mesocrystals were highly crystallized, as revealed from the HRTEM image in Fig. 2d. The clear lattice fringe of 0.46 nm was assigned to the (100) spacing of the rutile structure.

It is interesting that the rutile TiO_2 mesocrystals with different morphologies could be obtained from HNO_3 aqueous solution; the SEM and TEM images are shown in Fig. 3. The large-scale formation of particles with size 100–130 nm can be observed from the SEM images in Fig. 3a and b. High-magnification SEM (Fig. 3b) and TEM images (Fig. 3c) confirm that N-TiO_2-RM has a porous structure and is composed of tiny nanoparticles with diameter about 10–12 nm. The corresponding SAED pattern with single-crystal-like diffractions depicted in the inset of Fig. 3c suggest the mesocrystalline structure of the whole particle. Fig. 3d presents the HRTEM image of N-TiO_2-RM, the lattice fringe of 0.17 nm was assigned to the d_{211} spacing of rutile structure. Thus, the anion had a remarkable effect on the microstructures of the obtained rutile TiO_2 mesocrystals. This phenomenon was also found and discussed in our previous study.[34] The anion adsorption on TiO_2 nuclei is different, resulting in the formation of rutile TiO_2 mesocrystals with different microstructures.

Recently, a great deal of effort has focused on designing crystallographically oriented nanoparticle superstructures (mesocrystals) as promising electrode materials for lithium-ion batteries.[21,31] Such assemblies could possess the structural stability of microsized electrodes while exploiting the beneficial properties associated with nanosized electrodes and more reactive sites arising from the large surface area. Herein, we firstly investigate the Na-ion storage properties of rutile TiO_2 mesocrystals. Fig. 4a and b show the charge–discharge profiles at the selective cycles of C-TiO_2-RM and N-TiO_2-RM. Both specimens do not exhibit well-defined voltage plateaus during the charge or discharge process. This Na-ion storage behavior is similar to the anatase TiO_2 anode for NIBs.[31] Cyclic voltammetry curves (Fig. S2†) further revealed the Na-ion storage behavior for rutile TiO_2 mesocrystals. The irreversible side reactions with electrolyte at the first discharge process were also found from the CV measurements. A couple of broad and ambiguous redox peaks between 0.5 V and 0.9 V *vs.* Na/Na^+ in the subsequent cyclic sweeps are observed, probably corresponding to the reversible reduction of Ti^{4+} to Ti^{3+}.[23,30] This may suggest that the reaction between rutile TiO_2 and Na is a surface-confined charge-transfer process, which is similar to that of anatase TiO_2 anode for Na-ion storage.[28] It is notable that C-TiO_2-RM displays a higher discharge capacity of 685.7 mA h g^{-1} (599.7 mA h g^{-1} for N-TiO_2-RM) and a charge capacity of 379.3 mA h g^{-1} (268.3 mA h g^{-1} for N-TiO_2-RM). It could be due to the larger surface area of C-TiO_2-RM compared to N-TiO_2-RM (157 m^2 g^{-1} *vs.* 117 m^2 g^{-1}). Moreover, the rutile TiO_2 mesocrystals (C-TiO_2-RM) display a higher reversible capacity than that of anatase TiO_2 nanocrystals and nanorods for Na-ion storage.[23,26–28] Thus, it is very interesting that rutile TiO_2 exhibits more promising applications than that of anatase TiO_2 in Na-ion storage.

Fig. 4c presents the rate capability of C-TiO_2-RM, N-TiO_2-RM and commercial rutile TiO_2 nanoparticles (TiO_2-RNP) from 0.05 to 2 A g^{-1}. The BET surface area of the commercial rutile TiO_2 was about 34 m^2 g^{-1}, and the detailed characterizations were shown in our previous study.[35] All of the samples exhibited superior rate capability. The reversible discharge capacities of C-TiO_2-RM are 280 mA h g^{-1} at 0.1 A g^{-1} (230 mA h g^{-1} for N-TiO_2-RM) and 151 mA h g^{-1} at a relatively high rate of 2 A g^{-1} (132 mA h g^{-1} for N-TiO_2-RM), which is much larger than that of the rutile TiO_2 nanoparticles. It is found that titanium-based oxides (anatase TiO_2 and $Na_2Ti_3O_7$) show a low first coulombic efficiency when used as anode materials for NIBs. This large irreversible capacity could be mainly due to the occurrence of side reactions with electrolyte, solid–electrolyte interface (SEI)

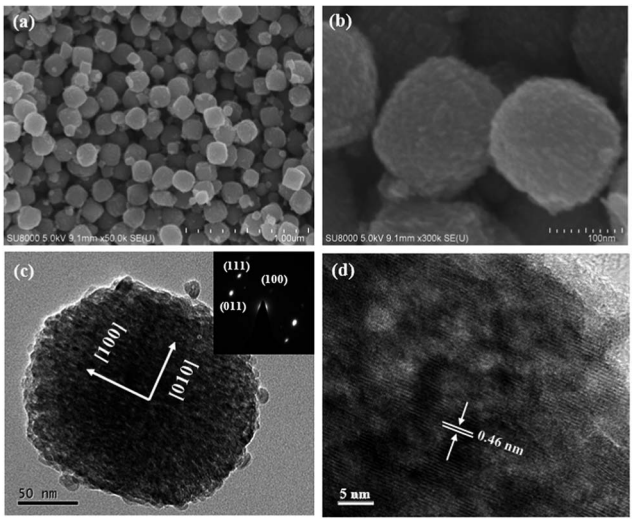

Fig. 2 SEM (a and b), TEM (c) and HRTEM (d) images of C-TiO_2-RM. The inset in (c) is the related SAED pattern from the whole nanoparticle.

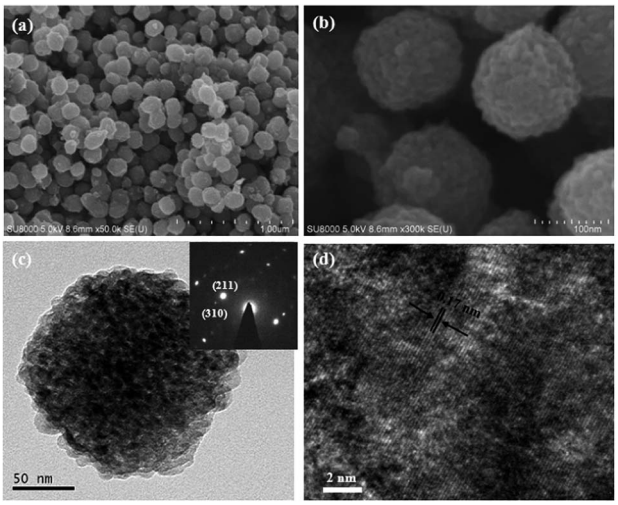

Fig. 3 SEM (a and b), TEM (c) and HRTEM (d) images of N-TiO_2-RM. The inset in (c) is the related SAED pattern from the whole nanoparticle.

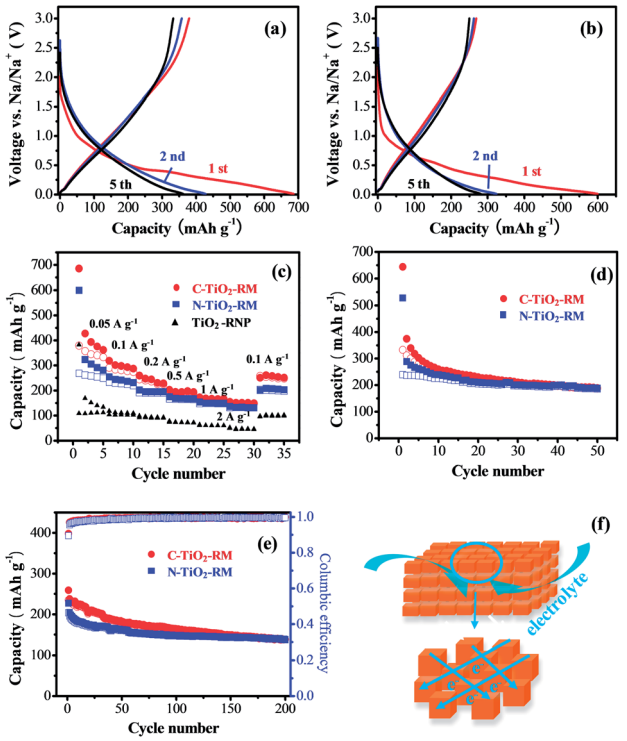

Fig. 4 Charge–discharge profiles of (a) C-TiO_2-MR and (b) N-TiO_2-MR at 0.05 A g^{-1}, (c) rate capability of C-TiO_2-MR, N-TiO_2-MR and rutile TiO_2 nanoparticles, (d) cycling performance of C-TiO_2-MR and N-TiO_2-MR at 0.1 A g^{-1}, (e) long cycling performance of C-TiO_2-MR and N-TiO_2-MR at 0.5 A g^{-1}, (f) scheme of a tentative electrochemical reaction process of TiO_2 mesocrystals (filled symbols: discharge capacity and open symbols: charge capacity).

formation and some irreversible structure change of the active materials.[23,26,28] Herein, it is worth mentioning that the coulombic efficiency at the first cycle for C-TiO_2-RM is 55% (45% for N-TiO_2-RM), which is much higher than that of TiO_2-RNP (28%). On the other hand, both the mesocrystals (N-TiO_2-RM and C-TiO_2-RM) exhibited remarkably higher capacity and better high rate capability than rutile nanoparticles. As depicted in Fig. 4f, crystallographically oriented mesocrystals possess a large surface area, nanoporous nature and few grain boundaries between the nanocrystals, which could provide a high level of accessibility for the electrolyte and more active sites, and allow fast electron and ion transport compared with the irregularly oriented nanoparticles.

Fig. 4d presents the cycling performance of C-TiO_2-MR and N-TiO_2-MR at 0.1 A g^{-1}; the capacities of 190 mA h g^{-1} and 188 mA h g^{-1} after 50 cycles could be retained, respectively. In order to test the long term cycling stability of the rutile mesocrystals, sodium-ion cells made from C-TiO_2-RM and N-TiO_2-RM were run at 0.5 A g^{-1} for 200 cycles, after aging at 0.1 A g^{-1} for 3 cycles. As presented in Fig. 4e, N-TiO_2-RM shows that reversible capacity starts at 204 mA h g^{-1} (235 mA h g^{-1} for C-TiO_2-RM) and is maintained at 138 mA h g^{-1} (also 138 mA h g^{-1} for C-TiO_2-RM) after 200 cycles at 0.5 A g^{-1}, as well as high coulombic efficiency, indicating a good cycling stability. It could be observed that the capacity decrease of N-TiO_2-RM mostly occurred at the initial cycle to the 20th cycle, whereas a good cycling stability was obtained in the following cycling process. On the other hand, N-TiO_2-RM showed a slightly better cycling stability than that of C-TiO_2-MR, which may be due to the larger pore size.

It is well known that Raman spectroscopy and XRD are effective measurements to investigate the structure of titanium dioxide, and the results are shown in Fig. 5. The curve of fresh electrode exhibits the typical Raman peaks of rutile TiO_2,[36] as presented in Fig. 5a. It is demonstrated that the rutile TiO_2 structure could be maintained during the discharge and charge process, although the intensities of all the peaks were lowered. This result is similar to the previous study.[29,30] Moreover, the morphology of the rutile TiO_2 mesocrystals remarkably remains even after the rate cycling test, as displayed in Fig. S4.† Therefore, the rutile TiO_2 mesocrystals exhibit not only a stable structure, but also a stable morphology during the Na-ion intercalation and extraction process, leading to good cycling stability.

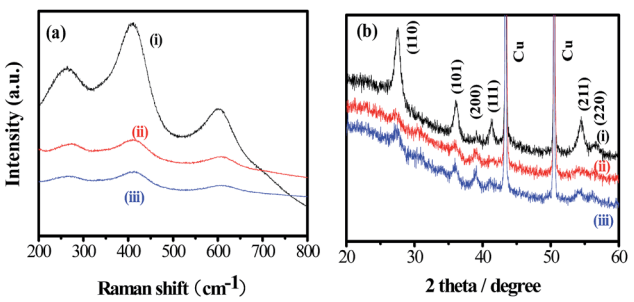

Fig. 5 (a) Raman and XRD patterns of N-TiO_2-MR electrode at various stages: (i) fresh, (ii) first discharge and (iii) first charge.

4. Conclusions

In summary, nanoporous rutile TiO_2 mesocrystals with a large surface area and tunable microstructures were successfully prepared *via* a facile synthesis route. Importantly, the rutile TiO_2 mesocrystals were firstly used as an anode material for sodium-ion storage. The rutile TiO_2 mesocrystals exhibited a high reversible capacity, superior rate capability and good cycling stability. This could be largely due to the unique architecture with nanoporous nature, large surface area and single-crystal-like structure, which could provide a high level of accessibility for the electrolyte and more active sites, and facilitate the fast electron and ion transport. Moreover, the rutile TiO_2 mesocrystals exhibit stable structure and morphology during the Na-ion intercalation and extraction process. Hence, the rutile TiO_2 mesocrystals could be a promising anode material for rechargeable Na-ion batteries. This study could also provide new insight in studying the TiO_2 anode and promote the development of advanced anode materials for Na-ion batteries.

Acknowledgements

This work was financially supported by National Natural Science Foundation of China (NSFC 21173049 and J1103303),

Research Fund for the Doctoral Program of Higher Education of China (RFDP 20133514110002), National Science Foundation of Fujian Province (2015J01042), Education Department of Fujian Province (JA14081) and Key Laboratory of Novel Thin Film Solar Cells, CAS.

References

1 J.-M. Tarascon, *Nat. Chem.*, 2010, **2**, 510.
2 H. Pan, Y.-S. Hu and L. Chen, *Energy Environ. Sci.*, 2013, **6**, 2338–2360.
3 Y. Kim, K.-H. Ha, S. M. Oh and K. T. Lee, *Chem.–Eur. J.*, 2014, **20**, 11980–11992.
4 N. Yabuuchi, K. Kubota, M. Dahbi and S. Komaba, *Chem. Rev.*, 2014, **114**, 11636–11682.
5 D. A. Stevens and J. R. Dahn, *J. Electrochem. Soc.*, 2001, **148**, A803–A811.
6 B. Jache and P. Adelhelm, *Angew. Chem., Int. Ed.*, 2014, **53**, 10169–10173.
7 Y. Xu, Y. Zhu, Y. Liu and C. Wang, *Adv. Energy Mater.*, 2013, **3**, 128–133.
8 A. Ponrouch, A. R. Goñi and M. R. Palacín, *Electrochem. Commun.*, 2013, **27**, 85–88.
9 Y. Liu, Y. Xu, Y. Zhu, J. N. Culver, C. A. Lundgren, K. Xu and C. Wang, *ACS Nano*, 2013, **7**, 3627–3634.
10 Y. Xu, Y. Zhu, Y. Liu and C. Wang, *Adv. Energy Mater.*, 2013, **3**, 128–133.
11 L. Wang, K. Zhang, Z. Hu, W. Duan, F. Cheng and J. Chen, *Nano Res.*, 2014, **7**, 199–208.
12 Z. Jian, P. Liu, F. Li, M. Chen and H. Zhou, *J. Mater. Chem. A*, 2014, **2**, 13805–13809.
13 C. Zhu, X. Mu, P. A. van Aken, Y. Yu and J. Maier, *Angew. Chem., Int. Ed.*, 2014, **53**, 2152–2156.
14 P. Senguttuvan, G. Rousse, V. Seznec, J.-M. Tarascon and M. R. Palacín, *Chem. Mater.*, 2011, **23**, 4109–4111.
15 S.-W. Kim, D.-H. Seo, X. Ma, G. Ceder and K. Kang, *Adv. Energy Mater.*, 2012, **2**, 710–721.
16 J. Yin, L. Qi and H. Wang, *ACS Appl. Mater. Interfaces*, 2012, **4**, 2762–2768.
17 W. Wang, C. Yu, Y. Liu, J. Hou, H. Zhu and S. Jiao, *RSC Adv.*, 2013, **3**, 1041–1044.
18 W. Wang, C. Yu, Z. Lin, J. Hou, H. Zhu and S. Jiao, *Nanoscale*, 2013, **5**, 594–599.
19 G.-N. Zhu, Y.-G. Wang and Y.-Y. Xia, *Energy Environ. Sci.*, 2012, **5**, 6652–6667.
20 Z. Hong, M. Wei, T. Lan, L. Jiang and G. Cao, *Energy Environ. Sci.*, 2012, **5**, 5408–5413.
21 Z. Hong and M. Wei, *J. Mater. Chem. A*, 2013, **1**, 4403–4414.
22 H. Ren, R. Yu, J. Wang, Q. Jin, M. Yang, D. Mao, D. Kisailus, H. Zhao and D. Wang, *Nano Lett.*, 2014, **14**, 6679–6684.
23 Y. Xu, E. M. Lotfabad, H. Wang, B. Farbod, Z. Xu, A. Kohandehghan and D. Mitlin, *Chem. Commun.*, 2013, **49**, 8973–8975.
24 H. A. Cha, H. M. Jeong and J. K. Kang, *J. Mater. Chem. A*, 2014, **2**, 5182–5186.
25 G. Qin, X. Zhang and C. Wang, *J. Mater. Chem. A*, 2014, **2**, 12449–12458.
26 K.-T. Kim, G. Ali, K. Y. Chung, C. S. Yoon, H. Yashiro, Y.-K. Sun, J. Lu, K. Amine and S.-T. Myung, *Nano Lett.*, 2014, **14**, 416–422.
27 X. Yang, C. Wang, Y. Yang, Y. Zhang, X. Jia, J. Chen and X. Ji, *J. Mater. Chem. A*, 2015, **3**, 8800–8807.
28 J. R. Gonzalez, R. Alcantara, F. Nacimiento, G. F. Ortiz and J. L. Tirado, *CrystEngComm*, 2014, **16**, 4602–4609.
29 H. Usui, S. Yoshioka, K. Wasada, M. Shimizu and H. Sakaguchi, *ACS Appl. Mater. Interfaces*, 2015, **7**, 6567–6573.
30 Y. Zhang, X. Pu, Y. Yang, Y. Zhu, H. Hou, M. Jing, X. Yang, J. Chen and X. Ji, *Phys. Chem. Chem. Phys.*, 2015, **17**, 15764–15770.
31 E. Uchaker and G. Cao, *Nano Today*, 2014, **9**, 499–524.
32 Z. Hong, M. Wei, T. Lan and G. Cao, *Nano Energy*, 2012, **1**, 466–471.
33 R. Q. Song and H. Cölfen, *Adv. Mater.*, 2010, **22**, 1301–1330.
34 Z. Hong, Y. Xu, Y. Liu and M. Wei, *Chem.–Eur. J.*, 2012, **18**, 10753–10760.
35 T. Lan, Y. Liu, J. Dou, Z. Hong and M. Wei, *J. Mater. Chem. A*, 2014, **2**, 1102–1106.
36 J. L. Gole, S. M. Prokes and O. J. Glembocki, *J. Phys. Chem. C*, 2008, **112**, 1782–1788.

